Hydrogen chloride adsorption on large defective PAHs modeling soot surfaces and influence on water trapping: A DFT and AIMD study

Bastien Radola, Ludovic Martin-Gondre, Sylvain Picaud, Marie-Thérèse Rayez, Jean-Claude Rayez

▶ **To cite this version:**

Bastien Radola, Ludovic Martin-Gondre, Sylvain Picaud, Marie-Thérèse Rayez, Jean-Claude Rayez. Hydrogen chloride adsorption on large defective PAHs modeling soot surfaces and influence on water trapping: A DFT and AIMD study. Chemical Physics, 2019, 523, pp.18-27. 10.1016/j.chemphys.2019.03.021 . hal-02989255

HAL Id: hal-02989255
https://hal.science/hal-02989255

Submitted on 5 Nov 2020

HAL is a multi-disciplinary open access archive for the deposit and dissemination of scientific research documents, whether they are published or not. The documents may come from teaching and research institutions in France or abroad, or from public or private research centers.

L'archive ouverte pluridisciplinaire **HAL**, est destinée au dépôt et à la diffusion de documents scientifiques de niveau recherche, publiés ou non, émanant des établissements d'enseignement et de recherche français ou étrangers, des laboratoires publics ou privés.

Hydrogen Chloride Adsorption on Large Defective PAHs Modeling Soot Surfaces and Influence on Water Trapping: a DFT and AIMD Study

Bastien Radola,[†,¶] Ludovic Martin-Gondre,[†] Sylvain Picaud,[*,†] Marie-Thérèse Rayez,[‡] and Jean-Claude Rayez[‡]

[†]*Institut UTINAM UMR 6213, CNRS/Université de Bourgogne Franche-Comté, Besançon, France*

[‡]*Institut des Sciences Moléculaires UMR 5255, CNRS/Université de Bordeaux, Talence, France*

[¶]*Current address: Laboratoire ICB UMR 6303, CNRS/Université de Bourgogne Franche-Comté, Dijon, France*

E-mail: sylvain.picaud@univ-fcomte.fr

Abstract

DFT calculations both at 0 K in energy optimization procedure and at finite temperature in *ab initio* molecular dynamics (AIMD) calculations are used to characterize the adsorption of the hydrogen chloride molecule on a carbonaceous cluster in which a carbon vacancy has been created by removing one carbon atom. This aims at modeling the defective surface of the small graphitic basic structural units that constitute soot nanoparticles, as experimentally evidenced. The results show that HCl can be easily dissociated at the vacancy site of the surface, resulting in the formation of a chlorinated site at the carbonaceous surface, which could have different structures depending on

the thermodynamics of the reactions. **Then, the resulting chlorinated carbonaceous surfaces are used as model substrates to characterize the first stages of the adsorption of water molecules on chlorinated soot. It is thus shown that adsorbed chlorine atoms may act as an efficient nucleation center for water trapping at the surface of soot**. These results represent a new step towards a better understanding of the soot behavior in industrial or domestic fire situations, as well as in marine atmospheric environment where oxidant and chlorinated species are ubiquitous.

Introduction

Aerosols are ubiquitous in the Earth's atmosphere and play a central role in recent climate evolutions as well as in public health.[1] Indeed, besides their direct effect on climate coming from their ability to scatter or absorb radiation, thus affecting the Earth's energy balance, aerosol particles can serve as nuclei for ice crystals and liquid droplets leading to an indirect effect on climate by impacting on cloud formation and precipitation.[2] Aerosols also participate in heterogeneous chemical reactions, thus modifying the abundance and distribution of trace gases in the atmosphere.[3] Moreover, their role in transporting irritant gases into the lungs after inhalation is now recognized to pose a major threat to public health.[1,4]

Among the huge variety of atmospheric aerosols that has to be better characterized, carbonaceous particles coming from fossil fuel or biofuel combustion deserve special attention because of the increasing importance of transport activities that contribute 20–25 % to the total anthropogenic emission of carbonaceous particles.[5] Although several different techniques have been used to characterize the formation, the structure and the physico-chemical properties of this so-called "combustor soot" from many years,[6,7] significant deficiencies still remain in our understanding of particle formation and aging, i.e., the evolution of soot in the atmosphere due to its reactivity with the surrounding gas species.[8]

Although the structure of combustor soot may depend on the process conditions, there

are some common general characteristics that are now well-recognized.[9–11] Thus, soot is made of primary particles of nanometer size, that are agglomerated to form more or less compact aggregates exhibiting random fractal structures and having sizes ranging from tens to hundreds of nanometers.[11–13] The soot primary particles exhibit a so-called turbostratic structure in which graphitic basic structural units (BSU) are randomly stacked on various spheres of increasing radii, as it has been evidenced by means of electron microscopy.[14–17] These BSUs are generally made of 2–3 aromatic layers with an interlayer space of about 3.4–4.2 Å,[18] and layer lengths ranging from less than one to a few nanometers.[15,17,19] Each layer can be viewed as a graphene-like sheet containing a certain amount of topological defects, the concentration of which being much more important at the surface than in the bulk of the primary particles.[17] These defects may be, for instance, heptagon-pentagon connections (i.e., similar to the so-called Thrower-Stones-Wales defects observed in various carbonaceous structures),[20,21] carbon vacancies or unsaturated carbon chains.[17] **In a general way, the high non-graphitic carbon ratios evidenced in the experiments point out the very defective nature of the outer graphene layers of the soot primary particles.[17] Thus,** heterogeneous chemistry at these defective sites may likely participate in the reactivity and hydrophilicity of soot[22,23] as it takes part in the reactivity of graphene and graphite surfaces.[24,25]

Characterizing the interaction of soot particles with the surrounding atmospheric gaseous species is of fundamental interest to better understand how soot aging may impact on their physico-chemical properties and, thus, modify the possible influence of soot on climate as well as on air pollution and health.[26–29] It is also mandatory when considering fire situations during which smokes, that can be viewed as mixtures of gases, vapors and particulates including soot, can be inhaled and, thus, transport irritant gases deeply into the respiratory system.[30]

Considering that i) hydrogen chloride (HCl) is one of the main chloride species produced in combustion of electrical elements and materials containing polyvinyl chloride (PVC) dur-

ing domestic and industrial fires,[31] II) chlorinated species are ubiquitous in the marine environment[32] where their interaction with soot particles emitted by shipping engines[33] can influence the formation of ship tracks[34] and, thus, modify the impact of the marine traffic on the terrestrial albedo,[33,35] III) the interaction between HCl and soot has been yet poorly characterized in the literature, we have recently studied the trapping of hydrogen chloride (HCl) and atomic chlorine ($Cl^{\bullet}$) at various sites of two polycyclic aromatic hydrocarbon (PAH) molecules ($C_{24}H_{12}$ and $C_{54}H_{18}$) by using density functional theory (DFT) methods with different functionals and basis sets.[36] Indeed, quantum chemical methods can provide such a detailed direct insight into the molecular level mechanism of chemical reactions that cannot be achieved by any experimental method itself. Moreover, since reactivity is usually a local phenomenon, its theoretical characterization does not require a detailed description of the whole soot particle that can, thus, be accurately represented by small carbonaceous clusters of size typically falling in the BSU size range. Thus, we use large PAH (C_xH_y) molecules as a proxy to model the surface of the graphene-like platelets that form the BSUs constituting soot primary nanoparticles, as in previous works based on quantum chemical calculations.[37–40]

Our results showed that the considered chlorine species can be either physisorbed or chemisorbed at the face or at the edge of the soot BSU, respectively. In addition, the theoretical characterization of the interaction of small water aggregates with the resulting chlorinated PAHs indicated that chlorine species may favor subsequent water adsorption on soot and, thus, participate in the hygroscopic behaviour of soot, for instance in smokes of industrial fires.[36]

Here, we go one step further by considering theoretically the interaction of HCl with a large PAH radical containing one carbon atom vacancy, i.e., a PAH species from which one carbon atom has been removed. This system aims at modeling the face of defective BSUs such as those recently evidenced at the surface of soot primary particles.[17] It is worth mentioning that carbon atom vacancies in the soot BSUs do not result from carbon atom removing from

already existing perfect graphene-like surfaces. Indeed, this process would require very high energy and can only be observed after, e.g., irradiating a carbonaceous surface with electrons or ions.[25] Rather, carbon atom vacancies at the surface of soot BSUs are likely directly formed during incomplete recombination of the soot precursors, as it has been evidenced in various numerical simulations of the soot formation at the atomic scale.[41–43]

We consider the specific situation of a defective BSU that we model by removing one central carbon atom from the large $C_{80}H_{22}$ molecule, thus forming a platelet made of fused carbonaceous rings arranged in a single atomic layer, that contains 79 carbon atoms, the edges of this BSU being saturated by hydrogen atoms. **Note that the largest size of this molecule is about 1.5 nm, which falls in the size distribution of real BSUs, as observed in the experiments.[17]** The optimized geometry, at the DFT level (see below), of this $C_{79}H_{22}$ radical is shown in Figure 1. Of course, this defective PAH is only a crude model of the soot surface. In particular, real soot BSUs are made of clusters of PAHs, separated by interlayer distances slightly larger than in graphite.[17] The influence of such clustering on the surface relaxation of the surface layer exposed to the gas phase is, however, difficult to take into account in the present DFT approach, in particular because this would involve a very large number of atoms **in the AIMD calculations**. Moreover, in a real soot, these PAH clusters are also tied together by carbon bridges that cannot be taken into account in our approach based on finite size BSUs.

To characterize the adsorption process of HCl on the $C_{79}H_{22}$ radical, we perform optimization calculations at the DFT level with the Gaussian 09 quantum chemistry package.[44] However, considering the large size of the system modeled here and the difficulty to find its minimum energy configurations, results of calculations at the semi-empirical Austin Model 1 (AM1) level[45] are also used as initial guesses for the subsequent search of the energy minima carried out with the more sophisticated DFT scheme. In addition, we perform *ab initio* molecular dynamics (AIMD) simulations at the DFT level using the Vienna *ab initio* simulation package (VASP)[46–49] because it has been proven to be an accurate tool to perform

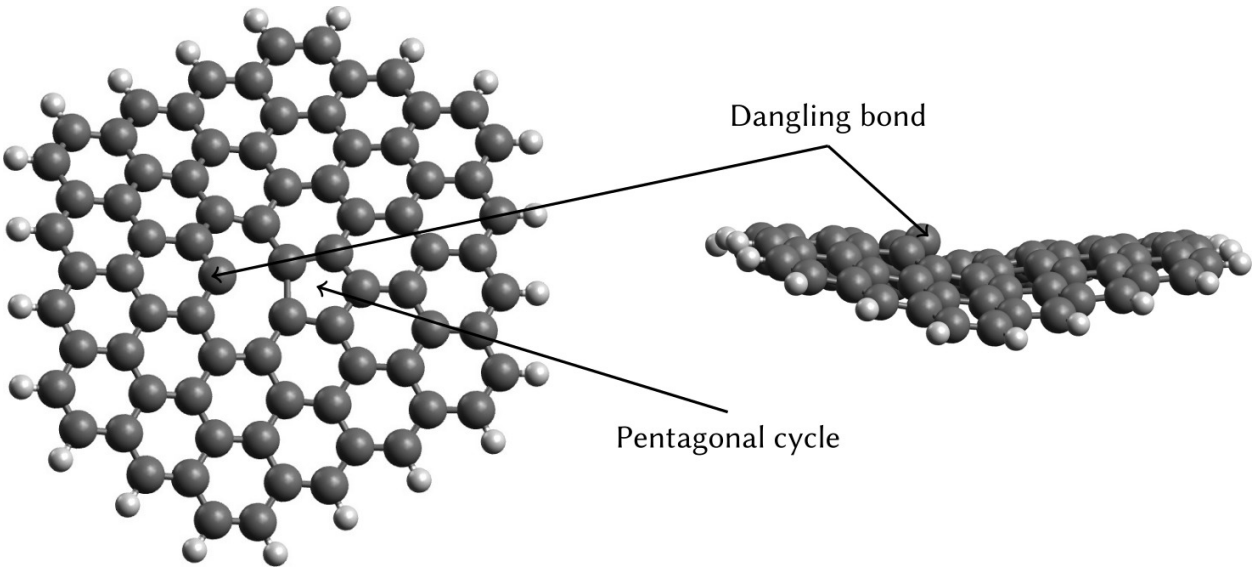

Figure 1: Geometry of the $C_{79}H_{22}$ radical after optimization with the PBE functional. This radical has been obtained from the $C_{80}H_{22}$ molecule by removing a central carbon atom. Note, at the vacancy site, the formation of a pentagonal cycle and the position out of the PAH plane of the carbon atom bearing the remaining free valence. Carbon and hydrogen atoms are represented as gray and white balls, respectively.

surface reactivity studies.[50] Indeed, using AIMD simulations allows to take into account the possible influence of the temperature on the HCl adsorption process. It also avoids a tedious explicit characterization of the possible energy barriers that may exist along the reaction paths of the adsorption process, as evidenced in previous studies of the reactivity of similar surfaces with H_2O and O_2 molecules.[23,51] .

Computational Details

In the AIMD calculations, the generalized gradient approximation (GGA) is adopted in the form of the Perdew, Burke and Ernzerhof (PBE) exchange correlation functional.[52] The electronic wave functions are expanded in a plane-wave basis set with an energy cut-off equal to 500 eV. In order to correctly describe the core electrons, pseudo-potentials generated using the projector-augmented-wave (PAW) method[53,54] are used. Calculations are done in a so-called super-cell so that the $HCl + C_{79}H_{22}$ system is isolated from its neighboring images in

a large cubic box, characterized by an edge length of 28 Å. This value has been optimized for our system, which means that using a larger box does not have any influence on the results. A k-points sampling of $1 \times 1 \times 1$, generated with the Monkhorst-Pack method,[55] is found to be sufficient with such a large simulation box.

In the AIMD study, HCl is initially placed right above the location of the carbon atom vacancy of the $C_{79}H_{22}$ radical. The initial orientation of HCl with respect to $C_{79}H_{22}$ is defined by the polar θ and azimuthal ϕ angles, as shown in Figure 2. Then, an initial velocity is given to the HCl molecule, in the direction of the vacancy site of $C_{79}H_{22}$. Two different directions of the velocity vector are defined, by considering the line connecting the center of mass of HCl and either the carbon atom having a free valence (position P_1) or the geometrical center of the defect (position P_2), i.e., the site of the missing carbon atom, evaluated by the mean position of its nearest neighbors. The initial distance between the center of mass of HCl and the positions P_1 or P_2 is set equal to 5 Å, a value corresponding to vanishing interactions between HCl and the surface at the beginning of the simulation runs. A time step of 1 fs is used for the ionic movements.

Then, the simulations involving both HCl and the defective carbonaceous cluster are carried out in the micro-canonical ensemble, in order to allow the HCl molecule to move freely without any periodic rescaling of its velocity by a thermostat, as it would be the case in the canonical ensemble.

It is worth noting that because of the high computational cost of AIMD calculations for the large system considered here, only quite short trajectories can be generated during the simulation runs within a reasonable time. To overcome this difficulty, a large number of various initial conditions (positions and velocities) should be considered in the simulations, to ensure a good exploration of the configuration space and, thus, the relevance of the results from a statistical point of view. However, considering a large set of fully randomized initial configurations would also be far too time-consuming and is therefore even not realistic. As a consequence, we rather use a simplified approach in which the initial configurations are

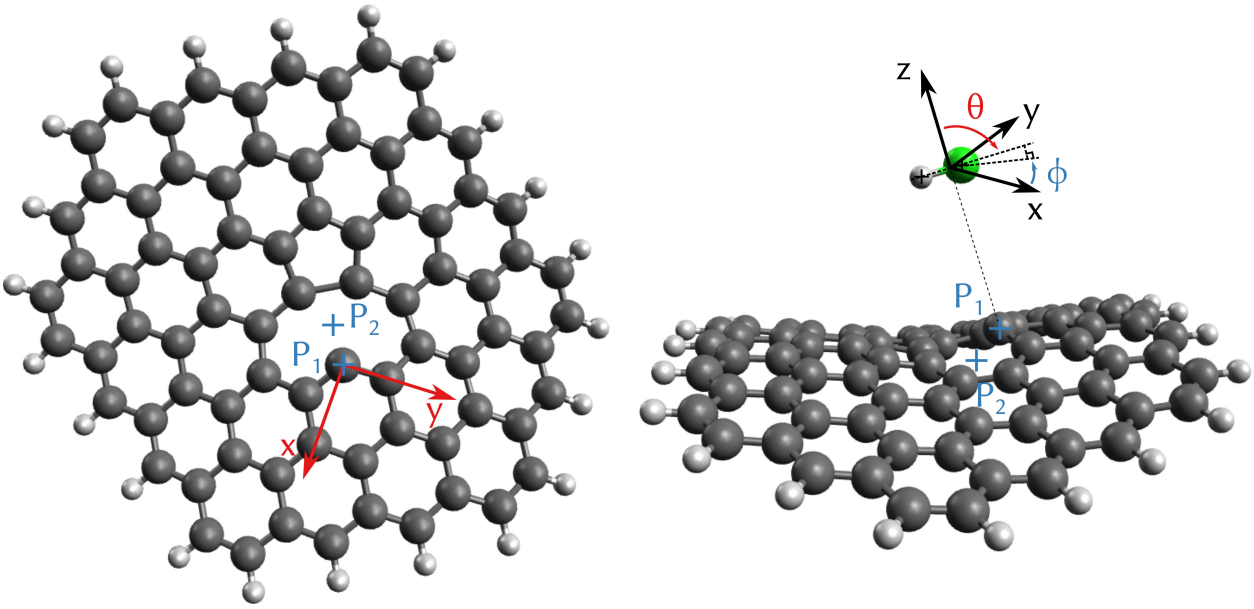

Figure 2: Illustration of the initial configurations of the AIMD simulation runs. The x, y and z axes are defined according to the direction of an arbitrarily chosen C−C bond and the mean plane of $C_{79}H_{22}$. The orientation of HCl in this frame is defined by the polar angle θ and the azimuthal angle ϕ. The initial velocity of HCl is directed towards a point of incidence that is either the carbon atom having a free valence (P_1) or the center of the defect (P_2). Carbon, hydrogen and chlorine atoms are represented as gray, white and green balls, respectively.

judiciously chosen to accurately sample the configuration space.

For the optimization runs with Gaussian, we use the well-known Becke, three-parameter, Lee-Yang-Parr (B3LYP) hybrid exchange-correlation functional,[56] which has already been used to study the adsorption of halogen atoms on graphene,[57] and the half-and-half hybrid functional BH&HLYP,[58] which has proven to correctly describe the structure of chlorine atom–benzene complexes.[59] Because of the large number of atoms in the systems under investigation, we only consider two relatively small basis sets in our calculations, namely the 6-31G(d,p) and the larger 6-311G(d,p) basis sets, for comparison. Moreover, optimization runs are also conducted with VASP (in the PBE scheme) in addition to AIMD simulations, for comparison with the results obtained with Gaussian using hybrid DFT functionals and atomic orbital basis sets.

Note that various initial conditions, i.e., different positions and orientations of the HCl molecules above the PAH radical, are considered in the calculations to increase the proba-

bility of finding the global energy minimum of the large systems under investigation.

Because the PAH radicals considered here are characterized by unpaired electrons, all the calculations with the Gaussian software are performed using the restricted open-shell (RO-DFT) scheme, to avoid any spin contamination that may affect the results of calculations in the unrestricted open-shell (U-DFT) approach.[60] When using VASP, both non spin-polarized (NSP) and spin-polarized (SP) calculations are performed, the former referring to a R-DFT scheme and the latter to an U-DFT scheme, in VASP terminology.[61]

Dissociative Adsorption of Hydrogen Chloride on a Large PAH Radical

Relaxation Study

We characterize by energy optimization the adsorption of the HCl molecule on the defective $C_{79}H_{22}$ radical presented in Figure 1. Because of the large size of the system considered, we first perform calculations at the semi-empirical level to get a rough picture of the potential energy surface corresponding to the HCl adsorption process. Thus, using AMPAC[62] with the AM1 method[45] and the restricted open-shell scheme, several configurations are obtained exhibiting similar energy values. All these structures correspond to final configurations where the HCl molecule is dissociated at the surface, the H and Cl atoms being chemically attached to the carbonaceous cluster.

Three main types of optimized structures are found at the AM1 level. In the first one, hydrogen and chlorine atoms are bound to two different carbon atoms, in *cis* (structure D_1) or *trans* (structure D_2) positions with respect to the surface of the carbonaceous cluster. The second type of optimized structures corresponds to adsorption of hydrogen and chlorine atoms both on the same carbon, structure G_1 being characterized by a position of the Cl atom as far as possible from the surface, whereas structure G_2 corresponds to the reverse

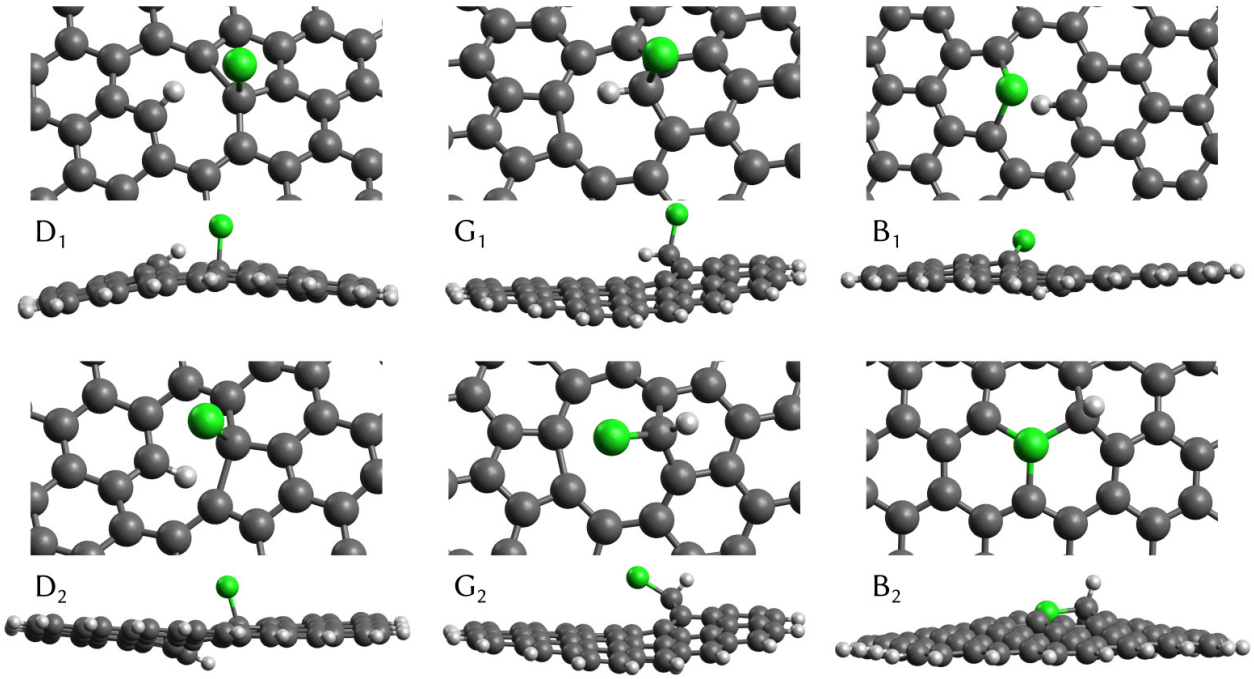

Figure 3: Pictures of the various optimized $C_{79}H_{23}Cl$ structures, obtained with the semi-empirical AM1 method after the dissociative adsorption of HCl on $C_{79}H_{22}$. For each structure, top and side views are given. Carbon, hydrogen and chlorine atoms are represented as gray, white and green balls, respectively.

situation. Finally, in structures of type B, the chlorine atom is located in a bridge position between two (B_1) or three (B_2) carbon atoms, the hydrogen being attached to a neighboring carbon. All these configurations are shown in Figure 3.

From an energetic point of view, the values of the enthalpy of formation, given in the first column of Table 1, indicate that structures D_1 and G_2 are less stable than structures D_2 and G_1 by about 0.5 eV. This can be related to steric effects. Indeed, in structure D_2, the H and Cl atoms are in a *trans* position with respect to the surface and, in structure G_1, the chlorine atom is attached as far as possible from the carbonaceous surface. The two most stable structures are B_1 and B_2 (with enthalpies of formation lower than those of G_1 and D_2 by about 0.5 eV), indicating that the number of Cl−C bonds that can be formed (two and three, for structures B_1 and B_2, respectively) is a key factor for the stabilization of the HCl dissociation product at the AM1 semi-empirical level of calculations.

HCl chemisorption on the defective carbonaceous surface leading to various possible stable

Table 1: Enthalpies of formation ΔH_f^0, calculated with the semi-empirical AM1 method, and adsorption energies E_{ads}, calculated at the DFT level, for the various optimized configurations of the $C_{79}H_{22}$ + HCl system. Four different functionals have been used in the DFT calculations, namely B3LYP, BH&HLYP, PBE and PBE-D2. Energy values are given for calculations performed with the 6-31G(d,p) basis set or the larger 6-311G(d,p) basis set (values in parentheses) and, for PBE and PBE-D2 calculations, using a plane wave basis set. Values are given in eV.

	ΔH_f^0	E_{ads}^{B3LYP}	$E_{ads}^{BH\&HLYP}$	E_{ads}^{PBE}	$E_{ads}^{PBE\text{-}D2}$
D_1	20.727	−1.380 (−1.321)	−1.627 (−1.582)	−1.157	−1.375
D_2	20.186	−1.555 (−1.497)	−1.831 (−1.783)	−1.301	−1.527
G_1	20.132	−1.996 (−1.934)	−2.346 (−2.289)	−1.718	−1.935
G_2	20.680	−1.218 (−1.168)	−1.561 (−1.516)	−1.045	−1.280
B_1	19.673	−0.832 (−0.801)	−1.030 (−1.004)	−1.050	−1.265
B_2	19.582	—	—	—	—

configurations, it is interesting to find the corresponding transition states and to characterize the possible existing energy barriers between the minima of the potential energy surface. Here, we use the implementation in AMPAC of the chain method[62] which is a technique specially devoted to the search of the transition states between local energy minima, again at the semi-empirical level with the AM1 method to save computational time, the relaxation of multiple point chain profiles being quite time consuming. The results (not presented) show that, with the exception of the D_1 to D_2 transition which exhibits a quite low energy barrier of 0.112 eV, all the other stable structures are separated from each other by high energy barriers larger than 1.8 eV. Thus, the various stable structures of the potential energy surface calculated for the HCl dissociation process on the defective carbonaceous surface are energetically isolated from each other, meaning that the corresponding system could easily be trapped in a local energy minimum at 0 K.

Given the approximations related to semi-empirical calculations, it is important to check, in a second step, the reliability of the results obtained with the AM1 method by performing a set of higher level calculations. Thus, we use the DFT method with various exchange-correlation functionals, including BH&HLYP, B3LYP and PBE, and various basis sets to characterize the minimum energy and the corresponding structure of the product of the HCl

adsorption process on the $C_{79}H_{22}$ radical. Note that the results of the previous semi-empirical calculations are used as a guide for this minimum energy search at the DFT level.

In the DFT calculations, the adsorption process, whether dissociative or not, of HCl on the defective surface is characterized by the adsorption energy E_{ads} defined as :

$$E_{\text{ads}} = E[C_{79}H_{22} + HCl] - E[C_{79}H_{22}] - E[HCl] \quad (1)$$

where $E[C_{79}H_{22} + HCl]$ corresponds to the total energy of the system after adsorption takes place whereas $E[C_{79}H_{22}]$ and $E[HCl]$ are the energies of the isolated reactants. These three energy values are obtained using the same calculation methods and parameters. The results of the DFT calculations (obtained with Eq. 1) are given in Table 1. From these energy values, conclusions similar to those obtained with the semi-empirical approach can be drawn. Indeed, the same type of structures, D, G, and B, are found, structures G_1 and D_2 corresponding to the lowest energy values, these two structures thus appear to be the most stable. However, in contrast with AM1 calculations, structure B_2 is not found in the DFT approach and structure B_1 corresponds to the configuration of highest energy. **Note also that including dispersion contributions in the calculations by using the PBE-D2 functional does not change these conclusions, the dispersion interaction adding however about** $-0.22\,\text{eV}$ **to the calculated adsorption energies.** This comparison clearly indicates that although calculations at the semi-empirical level could give interesting qualitative results for such large systems, the most stable structures have to be confirmed by the more sophisticated DFT method. It is worth mentioning that similar results are obtained with the various functionals and basis sets used in the DFT approach, at least in terms of comparative stability of the various structures found during the energy minimization process. This gives confidence in the present conclusions based on the DFT calculations.

Because the substrate considered in the present calculations has a finite size, structural changes (i.e., surface distortion) are evidenced upon dissociation of

Table 2: Interaction energies E_{int} and deformation energies E_{def}, calculated at the DFT level for the $C_{79}H_{22}$ + HCl system, with the PBE and PBE-D2 functionals. Values are given in eV.

	$E_{\text{int}}^{\text{PBE}}$	$E_{\text{int}}^{\text{PBE-D2}}$	$E_{\text{def}}^{\text{PBE}}[C_{79}H_{22}]$	$E_{\text{def}}^{\text{PBE-D2}}[C_{79}H_{22}]$
D_1	−2.697	−2.919	1.539	1.545
D_2	−2.558	−2.791	1.258	1.264
G_1	−2.627	−2.819	0.909	0.884
G_2	−2.584	−2.782	1.539	1.501
B_1	−3.038	−3.293	1.989	2.029

the HCl molecule as shown on the equilibrium configurations given in Figure 3. As a consequence, the adsorption energy, calculated as the difference between the energy of the most favorable configuration of the $C_{79}H_{23}Cl$ complex and the sum of the energies of the isolated, well-optimized, $C_{79}H_{22}$ and HCl species (see Eq. 1), accounts not only for the interaction energy between the HCl adsorbate and the substrate but also for the deformation energy of $C_{79}H_{22}$. It could thus be interesting to calculate separately the interaction energy, E_{int}, which corresponds to isolated $C_{79}H_{22}$ system with the atomic geometry of the $C_{79}H_{23}Cl$ complex. In this approach, the difference between E_{ads} and E_{int} is termed the deformation energy E_{def}.[63] Using both PBE and PBE-D2 functionals, the deformation energy for the various stable configurations given in Figure 3 varies between about 0.9 to about 2.0 eV, the lowest value being for the G_1 configuration, whereas the largest one is for the B_1 structure. These results indicate that a large part of the differences between the adsorption energies corresponding to the various stable configurations comes from the deformation of the PAH upon HCl dissociation. By contrast, the differences in the interaction energies only lie within a 0.5 eV range between the various stable configurations (see Table 2). Thus, the results obtained here may depend on the deformation of the surface, i.e., on the size of the PAH considered.

As a consequence, to quantify the effect of the size of the PAH, we also per-

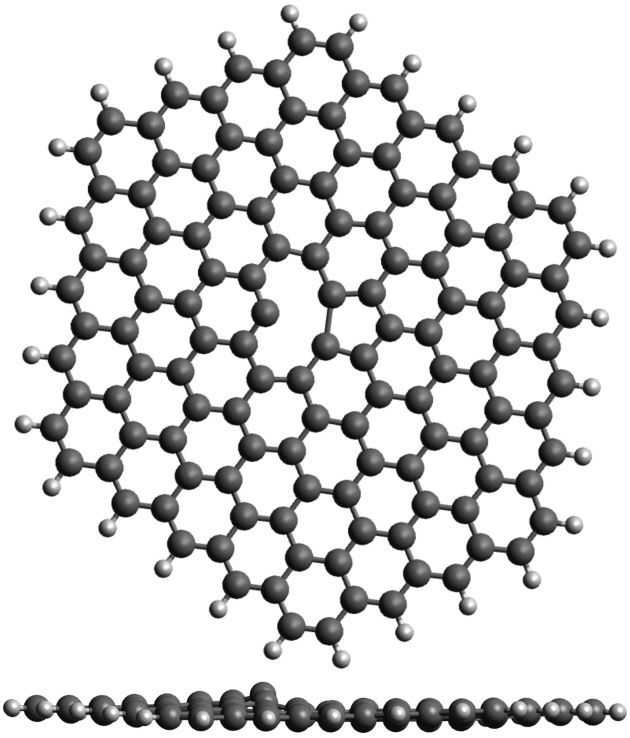

Figure 4: Geometry of the $C_{129}H_{28}$ radical after optimization with the PBE functional. Carbon and hydrogen atoms are represented as gray and white balls, respectively.

form a set of optimizations at the DFT level on the larger $C_{129}H_{28}$ radical, shown in Figure 4. The corresponding results obtained with the PBE and PBE-D2 functionals are given in Table 3. They show that the adsorption energies calculated on the $C_{129}H_{28}$ system are larger, in absolute value, than those obtained on $C_{79}H_{22}$ by about $0.2\,\mathrm{eV}$ for D structures, whereas they are very similar for G structures. Anyway, G_1 remains the configuration corresponding to the lowest HCl adsorption energy, followed by D_2, irrespective of the substrate size. Note also that the B_1 configuration is not found stable on this large PAH radical.

In addition, to model larger carbonaceous sheets, we also perform similar calculations by keeping fixed the carbon and hydrogen atoms located at the edge of the $C_{129}H_{28}$ species, as if these edge atoms are maintained in their positions by surrounding atoms within a larger BSU. The corresponding results given in the last two columns of Table 3 still indicate that G_1 and D_2 correspond to the

Table 3: Adsorption energies E_{ads}, calculated at the DFT level using the PBE and PBE-D2 functionals, for the adsorption of HCl on the $C_{79}H_{22}$ and $C_{129}H_{28}$ radicals. In addition, results are also given for a $C_{129}H_{28}$ substrate for which the carbon and hydrogen atoms at the edge have been kept fixed during the calculations (last two columns). Values are given in eV.

	$C_{79}H_{22}$		$C_{129}H_{28}$		$C_{129}H_{28}$ fixed edges	
	E_{ads}^{PBE}	$E_{ads}^{PBE\text{-}D2}$	E_{ads}^{PBE}	$E_{ads}^{PBE\text{-}D2}$	E_{ads}^{PBE}	$E_{ads}^{PBE\text{-}D2}$
D_1	−1.157	−1.375	−1.330	−1.533	−1.136	−1.361
D_2	−1.301	−1.527	−1.534	−1.765	−1.174	−1.405
G_1	−1.718	−1.935	−1.734	−1.956	−1.676	−1.891
G_2	−1.045	−1.280	−1.054	−1.289	−0.979	−1.209

lowest adsorption energies.

Up to this point, only singlet state systems have been considered in our study. Some additional calculations are thus performed by considering triplet state systems. Here, triplet state calculations give systematically higher adsorption energies than singlet state ones, the energy differences ranging from 0.13 eV for D_2 to 0.80 eV for G_2. Thus, we can reasonably conclude that the most stable structures for the product of the HCl adsorption process on the $C_{79}H_{22}$ radical correspond to singlet states.

AIMD Study

To get further insights on the reactivity of HCl with $C_{79}H_{22}$, we also perform an AIMD study using VASP with the PBE functional, thus allowing us to take into account the dynamic effects on the adsorption process. As it has been shown above for the energy optimization procedure, these functional and plane wave basis set give results in global accordance with those obtained from hybrid functionals and atomic orbital basis sets, as implemented in Gaussian (see Table 1).

The first set of calculations is devoted to a carbonaceous surface at an initial temperature of 0 K with an initial kinetic energy of the HCl molecule equal to 0.04 eV, which corresponds roughly to the average translational kinetic energy for a HCl molecule at 300 K. Let us first detail the results obtained when the initial velocity vector is directed perpendicular to the

surface, and the incidence point is chosen to be P_1 (see Figure 2). In this case, 5 values of the angle θ (0°, 45°, 90°, 135° and 180°) and 4 values of the angle ϕ (0°, 90°, 180° and 270°) are considered because they are roughly representative of the different initial orientations that the HCl molecule can have with respect to the surface. The simulation results show that quite short simulation runs (between 1 and 3 ps-long) are sufficient to obtain final structures similar to those previously evidenced with energy optimization techniques at the DFT level of calculations. Note, however, that in addition to the expected dissociative adsorption of HCl at the defect site of the surface, some physisorption states are also obtained in the AIMD runs, as well as some situations in which the HCl molecule is reflected back to the gas phase, i.e., no adsorption process is observed. Such a situation is considered as the final result of a simulation run when the distance between the HCl molecule and the surface becomes greater than 4.25 Å. Overall, the AIMD results show a strong influence of the initial orientation of the HCl molecule on the final product of the reaction with the surface. This dependence of the simulation results on the initial orientation of HCl is presented in Figure 5, as a diagram giving the final configuration of the system at the end of the AIMD runs, as a function of the θ and ϕ angles. As it is shown on this diagram, various configurations are obtained, namely D_1 or G_1 structures, reflection of the HCl molecule back to the gas phase (R) and physisorption (P).

Nevertheless, the results shown in Figure 5 indicate that most of the simulations end with the D_1 or the G_1 structure, depending mainly on the θ values. Indeed, structure G_1 is preferentially obtained starting with small θ values, i.e., initial configurations in which the hydrogen atom of HCl points towards the defective site of the $C_{79}H_{22}$ radical, whereas structure D_1 is obtained at intermediate θ values, i.e., when the HCl molecule is initially oriented more or less parallel to the surface. When the chlorine atom points towards the $C_{79}H_{22}$ radical (a situation corresponding to initial large θ values), most of the runs end with the HCl molecule reflected back to the gas phase. Angle ϕ has a much weaker influence on the results of the AIMD runs, except for the value $\theta = 135°$, for which in Fig. 5a for

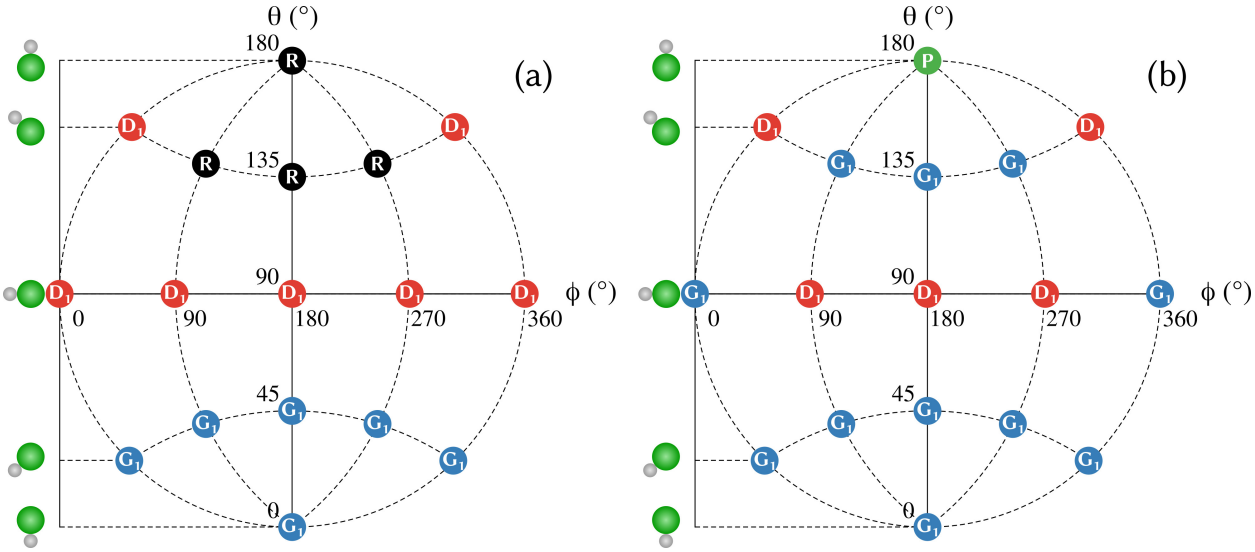

Figure 5: Results of the AIMD simulations at an initial surface temperature of $T = 0\,\mathrm{K}$, for an initial kinetic energy of HCl of $E_{\mathrm{init}} = 0.04\,\mathrm{eV}$ and at an incidence angle of 0°, depending on the initial orientation angles of HCl with PBE (a) and PBE-D2 (b) functionals. Colored circles correspond to different products with the following correspondences: structures G_1 (blue) and D_1 (red), reflection to the gas phase R (black) and physisorption P (green).

instance, either the structure D_1 or the R situation is obtained depending on the initial value of the ϕ angle.

Note that calculations are performed with (Figure 5b) or without (Figure 5a) taking into account the possible dispersion effects that are thus investigated by considering the DFT-D2 method,[64] which adds a long-range empirical dispersion correction to the exchange-correlation functional. Indeed, in our AIMD simulations, the incoming HCl molecule is initially located quite far from the carbonaceous surface, where long-range dispersion contributions to the energy can possibly play a significant role. However, taking into account the dispersion corrections by using the PBE-D2 functional does not have a determining effect in most cases, except for the occurrence of the physisorption state which is observed only when explicit dispersion contribution is considered in the exchange-correlation functional. In addition, it appears that this dispersion contribution tends to statistically favor structure G_1 at the expense of both structure D_1 and R situation. In this case, the simulation time required to observe the formation of structure G_1 depends on the θ angle and increases typically from

0.6–0.7 ps to 3–4 ps at small and large angle values, respectively. **It is worth mentioning that nudged elastic band (NEB)[65] calculations (not presented) clearly indicate the lack of any noticeable energy barrier along the reaction paths leading to the formation of G_1 and D_1 structures. This is in contrast with the dissociation of water molecule on carbon atom vacancies at the surface of graphite[66] or large PAHs,[51] which is characterized by energy barriers of about** 0.8 eV**.**

Finally, note that some simulations are also carried out using the spin-polarized scheme. A careful examination of the spin states during the course of these AIMD calculations unambiguously shows that initial and final systems are open state singlets, as already obtained in static DFT calculations. In addition, using a spin-polarized scheme does not show any influence on the AIMD results, with however a strong penalty in terms of simulation times which are more than doubled.

Other values of the initial kinetic energy of the HCl molecule are also considered for comparison: 0.005 eV, 0.5 eV and 1 eV. The influence of E_{init} is found to be quite weak at low θ values, where the products are of type G_1. However, at an incidence energy of 0.5 eV or more, the reflection process becomes a dominant exit channel for the HCl molecule, at θ values equal or higher than 90°, instead of the formation of the D_1 structure. This might be related to the fact that the formation of structures D leads to a reorganization of the carbonaceous surface, as evidenced in the relaxation study (see above), during which the $C_{79}H_{22}$ radical flattens after the breaking of the pentagonal cycle near the atomic vacancy. Note that the formation of structure D_1 also requires longer equilibration times (for instance, between typically 1 and 1.3 ps for an incident energy of 0.04 eV, instead of 0.6–0.7 ps for the formation of structures G_1 in the same conditions).

For comparison, some simulations are also carried out with different initial orientations of the HCl velocity vector. Considering our previous discussion showing that the dispersion contribution to the potential energy can impact on the simulation results, we use the PBE-D2 functional for all these calculations. For an incident orientation of the velocity vector equal

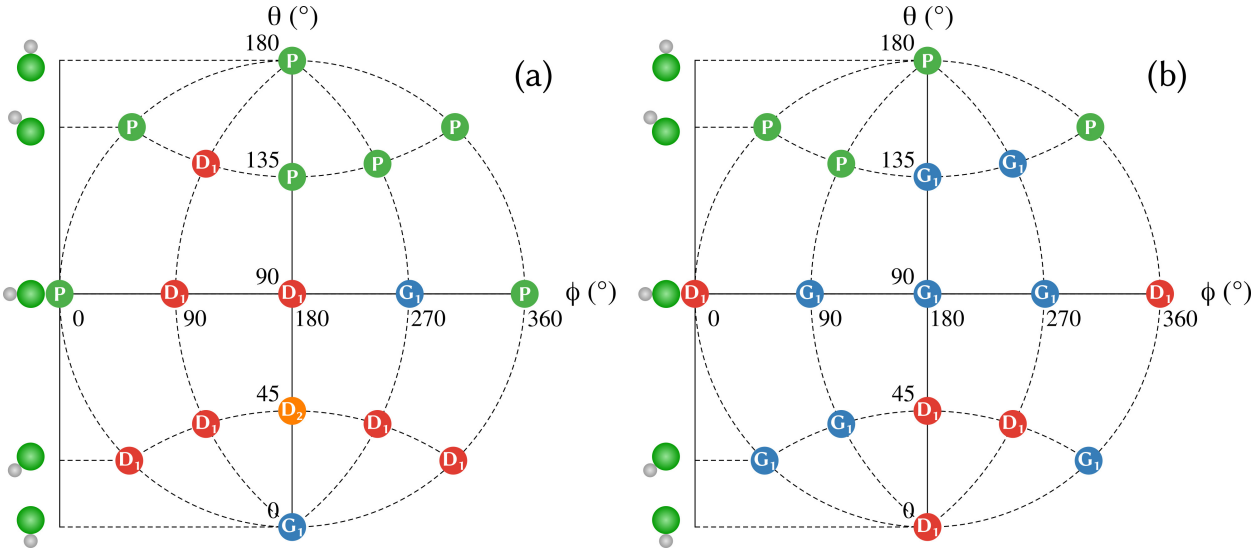

Figure 6: Results of the AIMD simulations with the PBE-D2 functional for an initial surface temperature of $T = 0\,\mathrm{K}$, an initial kinetic energy of HCl of $E_{\mathrm{init}} = 0.04\,\mathrm{eV}$ and at an incidence angle of 30°. HCl is approaching to the free valence site (P_1) either from the side where the pentagonal cycle is, or (b) from the opposite side. Colored circles correspond to different products with the following correspondences: structures G_1 (blue), D_1 (red) and D_2 (orange), reflection to the gas phase R (black) and physisorption P (green).

to 30°, the results show larger occurrences of the physisorption state, particularly when the chlorine atom is initially closer to the surface than the hydrogen atom, whereas mainly D_1 and G_1 structures are obtained for other initial orientations of HCl (Figure 6). Note that the structure D_2 also appears once in these results (Figure 6a). When considering a grazing incoming trajectory of HCl (i.e., an incidence angle of 60° or more), the reflection process becomes dominant. This can be expected considering that, in this case, HCl encounters first the non defective part of the carbonaceous cluster and, thus, bounces without interacting with the defect zone.

Likewise, additional calculations are conducted with a different point of incidence; thus, the initial velocity vector of the HCl molecule is directed towards the point P_2 located at the center of the carbon atom vacancy of the carbonaceous cluster (see Figure 2). In this case, AIMD results show a strong predominance of the structure D_1 in the set of final configurations, whereas no structure G_1 is obtained. Interestingly, the structure D_2 is also scarcely evidenced in these results, at high incidence energy only. Anyway, the main conclusion of

this AIMD study at a surface temperature of 0 K is the predominance of the structures G_1 and D_1 as the main products of the HCl adsorption, with an almost equivalent probability of formation. It is worth mentioning that neither structure G_2 nor structures of type B are obtained in these calculations. This is not very surprising because these structures correspond to higher energies, as shown in optimization procedure. Moreover, the structure D_2 appears only scarcely as the final product of the HCl dissociation in AIMD calculations. This could be due to the complex coupling between all degrees of freedom (positions and momenta) involved in the phase space which can favor the formation of D_1 with respect to D_2 in AIMD calculations. But we cannot exclude that longer AIMD runs or higher incidence energy would have been required to evidence the formation of structure D_2 because it corresponds to a *trans* configuration in which chlorine and hydrogen atoms are adsorbed at both sides of the carbonaceous cluster, an adsorption process that requires a reorganization of the surface structure.

In a second step, the influence of the surface temperature in the AIMD simulations is taken into account following a similar procedure to that used by Nattino et al..[67,68] First, AIMD simulations are performed by considering only the $C_{79}H_{22}$ radical, in the canonical ensemble. At the end of this (N, V, T) simulation run, a set of velocities are assigned to the carbon and hydrogen atoms, corresponding to the desired temperature T. These velocities are then used as initial velocities for the subsequent (N, V, E) simulations including the HCl molecule. Three initial surface temperature values are considered, namely 100 K, 200 K and 300 K, which means in fact that three different sets of velocities have been assigned to the surface atoms at the beginning of the simulations. Note that our AIMD microcanonical simulations are beyond the frozen surface approximation. Indeed, the surface atoms are not fixed during the simulations allowing for a more realistic description of the interaction between the HCl molecule and the $C_{79}H_{22}$ surface with permitted exchange energy.

Our results show that an initial surface temperature of $T = 100$ K does not significantly impact on the generated configurations. Indeed, AIMD trajectories lead to D_1 and G_1 struc-

tures as well as reflections back to the gas phase, as exhibited in the diagrams corresponding to simulation results at 0 K (Figure 5). Strong changes are however obtained at an initial surface temperature of $T = 200$ K, for which HCl is finally found in the gas phase without any adsorption, irrespective of its initial orientation, except for $\theta = 0°$, i.e., when the hydrogen atom points directly towards the $C_{79}H_{22}$ surface. In this case, simulation results show the favored formation of the G_1 structure. At an initial surface temperature of 300 K, no dissociative adsorption is observed anymore, irrespective of the initial conditions (orientation angle and incidence energy). This might be related to the large thermal motions of the carbonaceous surface at this temperature, which complicate the finding of an efficient reaction path for the dissociative adsorption of the HCl molecule. Note, however, that the number of initial configurations considered in the present AIMD simulations is rather limited for the reasons explained above, and it cannot be claimed that such dissociative reaction path does not exist, although we did not find it. Moreover, it should also be kept in mind that the model used for the surface is quite simple, and the thermal behavior of such a small carbonaceous system cannot be simply extrapolated to the very large, real, carbonaceous nanoparticles forming soot. In particular, the defective BSUs constituting soot nanoparticles **are made of clusters of graphene-like sheets and they are also tied together**, a feature which certainly complicate the modeling of the surface temperature and the corresponding thermal behavior. This is clearly one of the main limitation of our modeling at finite temperature and, for these reasons, we do not considered in our approach the higher temperatures that could be encountered in industrial fire situations.

Adsorption of Water Molecules on the Chlorinated Carbonaceous Surface

The previous sections of this paper have been devoted to the dissociative adsorption of hydrogen chloride on defective carbonaceous cluster modeling the surface of soot BSUs. The

results of both energy optimization procedure and AIMD simulations have indicated that the most stable chlorinated surfaces resulting from the HCl dissociation on the defective carbonaceous $C_{79}H_{22}$ radical are the G_1 and D_1 configurations. In this section, we focus on the interaction of these chlorinated surfaces with water, to characterize their ability to act as water nucleation centers. Thus, energy optimization is performed using static DFT calculations at the B3LYP/6-31G(d,p) level with Gaussian, following the procedure used in previously published works.[23,51,69]

From 1 to 6 water molecules are initially located at the vicinity of the chlorine atom of the $C_{79}H_{23}Cl$ surface and several relaxation runs are performed, each of them starting from slightly different initial configurations in order to optimize the probability of finding the structure of lowest energy. Because the requested time to reach this minimum dramatically increases with the number of degrees of freedom and, hence, with the number n of water molecules, we do not consider more than $n = 6$ water molecules in the calculations. However, as it will be shown below, it is not necessary to go beyond this value because any additional water molecule tend to adsorb on the water already attached to the surface, without interacting directly with the substrate. Clearly, for n values larger than 5–6, this situation corresponds to adsorption of water on water.

The results for water adsorption on the structure G_1 are illustrated by the snapshots of the corresponding equilibrium configurations given in Figure 7. They show that the first water molecule (calculations performed with $n = 1$) adsorb directly on the chlorinated site of the surface, oriented nearly parallel to the surface and with one hydrogen atom pointing towards the chlorine atom. The corresponding adsorption energy is $E_{\text{ads}} = -0.210\,\text{eV}$, similar to the energy of a hydrogen bond establishing in liquid water ($-0.241\,\text{eV}$).[70] When $n = 2$, the two water molecules are adsorbed in the close vicinity of the chlorinated site of the surface, with one hydrogen bond formed between the two molecules. This equilibrium configuration also corresponds to the optimization of one donor H-bond with chlorine for one water molecule, and one acceptor H-bond with the surface hydrogen for the second water molecule. For

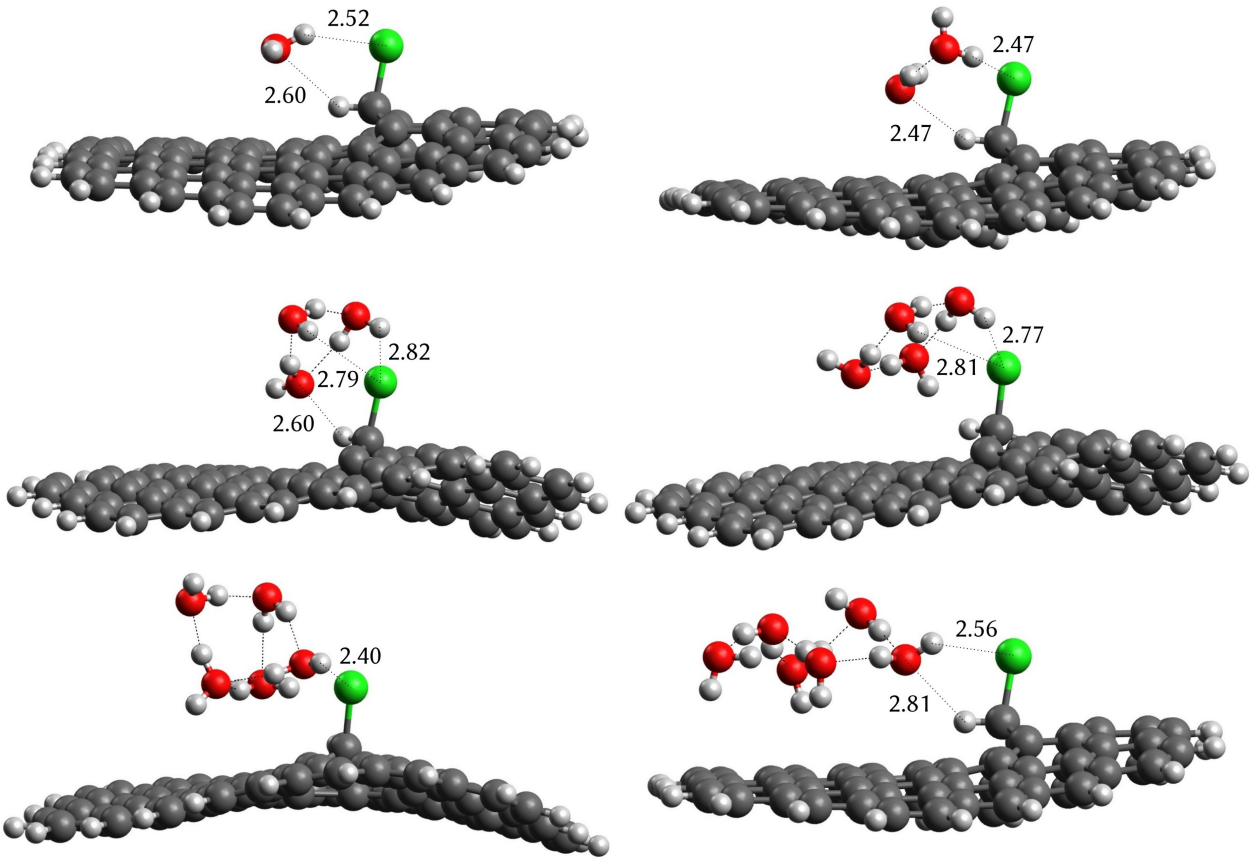

Figure 7: Snapshots of the water adsorption of n water molecules on the structure G_1 of $C_{79}H_{23}Cl$, with n ranging from 1 to 6. Numbers on the snapshots correspond to interatomic distances given in Å. Carbon, hydrogen, chlorine and oxygen atoms are represented as gray, white, green and red balls, respectively.

larger n values, the energy minima correspond to a subtle balance between hydrogen bonding with the chlorinated site of the surface and between the water molecules themselves. As a consequence, the usual structures of the water trimer and tetramer are clearly identified in Figure 7 for $n = 3$ and $n = 4$, as being very stable structures for water aggregates attached to the chlorinated site. Very similar configurations of the water aggregates are found when considering the structure D_1 of the chlorinated surface and, thus, the corresponding snapshots are not shown.

On a more quantitative level, it is interesting to compare the adsorption energies E_{ads} of water molecules on the two chlorinated carbonaceous surfaces (structures D_1 and G_1), and also on various oxygenated carbonaceous surfaces. Thus, a few examples of oxygenated

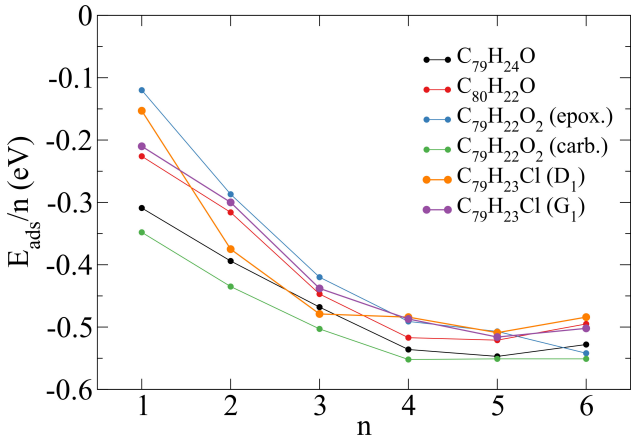

Figure 8: Adsorption energies per water molecule E_{ads}/n for the two chlorinated carbonaceous surfaces (D_1 and G_1 structures) considered here and for three different oxygenated carbonaceous surfaces taken from the literature. Structure and adsorption energy are computed at the B3LYP/6-31G(d,p) level.

carbonaceous clusters are considered as models of oxidized soot surfaces. They are taken from the literature and include an epoxy site located on a perfect surface (cluster $C_{80}H_{22}O$),[23] a carbonyl site issued from the dissociation of a water molecule at a carbon atom vacancy site (cluster $C_{79}H_{24}O$),[51] and a double oxygenated site, formed after the dissociation of one O_2 molecule at a carbon vacancy site. This last structure is characterized by the formation of one epoxy site on one face, and one carbonyl site on the other face of the carbonaceous cluster modeling the reactive surface.[69] However, because the results of the literature have been obtained using different calculation methods, here we re-optimize the adsorption energies of up to 6 water molecules on these various oxygenated surfaces with the same method used for characterizing the adsorption on the chlorinated carbonaceous surfaces. Then, the corresponding adsorption energy per water molecule E_{ads}/n is given in Figure 8, as a function of n.

Overall, the curves shown in Figure 8 exhibit a very similar behavior, i.e., the adsorption energy per water molecule decreases when the number n of adsorbed water molecules increases, thus showing that water trapping on these chlorinated and oxygenated surfaces is an energetically favorable process. However, at the very beginning of the water adsorption process, i.e., up to $n = 3$, it appears that the most attractive site for water adsorption is

the carbonyl site of $C_{79}H_{22}O_2$, whereas the less attractive one is the epoxy site of $C_{79}H_{22}O_2$. For larger n values, adsorption energies converge to very similar values of about -0.5 eV per water molecule, indicating that any additional water molecule adsorbed after the fifth one tends to stick on the previously adsorbed water molecules without significant interaction with the surface. This convergence of the results indicates that it is not necessary at this point to characterize the adsorption energy of larger water aggregates, especially because finding the lowest energy structure is an increasingly difficult challenge when n increases. Anyway, the present results show that chlorinated and oxygenated structures should behave similarly with respect to the first steps of the water nucleation process on a carbonaceous surface, as already stated in our previous study.[36] Thus, both chlorinated and oxygenated sites could participate in the hydrophilicity of soot, in fire situations as well as in marine atmospheric environment.

Conclusion

In this paper, we investigate the adsorption of the hydrogen chloride molecule on a carbonaceous cluster in which a carbon vacancy has been created by removing one carbon atom, to model the defective surface of the small graphitic basic structural units that constitutes soot nanoparticles. First-principles calculations at the DFT level of theory are performed, for the energy optimization of the reaction products at 0 K and for AIMD simulations at zero and finite temperatures. The results show that HCl can be easily dissociated at the vacancy site of the surface, resulting in the formation of a chlorinated site at the carbonaceous surface, that could have different structures depending on the conditions of the reaction. In particular, it appears from the results of the AIMD simulations that the surface temperature could play a crucial role in controlling the formation of the reactions products. Indeed, high temperature values could be requested to overcome energy barriers along the reaction paths, while sufficiently low surface temperature would avoid the incoming molecule to be sent back to the

gas phase. However, it should be mentioned that the influence of the temperature cannot be taken into account on a realistic way without considering the whole structure of the soot nanoparticle or, at least without performing, for instance, parameterized Langevin dynamics allowing accurate treatment of the energy exchanges between the incoming molecule and the substrate, which is far beyond the scope of this paper. Anyway, the present study confirms our previous conclusions[36] that soot surface could be reactive with respect to the adsorption of chlorinated species, at least under certain thermodynamical conditions.

Moreover, it should also be mentioned that the availability of unsaturated sites for HCl adsorption depends on the aging of the soot particle after its formation and on the composition of the gas phase in contact with soot. Indeed, as already shown in previous theoretical studies, unsaturated sites are also strongly reactive with respect to oxygenated species[51,69] and a thorough characterization of the competitive adsorption between different species on these sites remains to be performed.

In a second step, we characterize the adsorption of water molecules on chlorinated carbonaceous surfaces and show that these surfaces could favor water nucleation on soot, as oxygenated surfaces do. From the present results, it can be inferred that the two main factors impacting on the soot hydrophilicity are the modification of its surface by the interaction with chlorinated or oxygenated molecules, and the surface distribution of the resulting chlorinated and oxygenated sites, rather than the chemical nature of these sites. Note that the first factor would depend not only on the exothermicity of the corresponding reactions but also on their kinetics (which however has not been taken into account in the present approach). The second one is related to the fact that water nucleation on graphitic surfaces proceeds by coalescence of the growing water aggregates that are tied to the trapping sites of the surface, a process that is, of course, strongly influenced by the distance between these trapping sites.[71–73]

Although the reported data are far to provide a realistic model for the chemistry in

industrial or domestic fire situations, they can, at least qualitatively, be related to some experimental observations on the hydrophilic behavior of soot produced in industrial installations.[74–76] The present study thus represents an additional step for a better understanding of the soot behavior in industrial or domestic fire situations, as well as in the marine environment where chlorinated species and atmospheric oxidants are ubiquitous.

Acknowledgement

Calculations were performed using the computing resources of the Mésocentre de Calcul, a regional computing center at Université de Franche-Comté, DNUM CCUB, the computing center of Université de Bourgogne, and Gaudi, a computer at the Institut des Sciences Moléculaires (ISM) of Bordeaux. The Région Franche-Comté is gratefully acknowledged for its financial support. Collaboration between UTINAM and ISM has been developed in the framework of the french GDR CNRS 3622 (GDR SUIE).

References

(1) Pöschl, U. Atmospheric Aerosols: Composition, Transformation, Climate and Health Effects. *Angew. Chem. Int. Ed.* **2005**, *44*, 7520–7540.

(2) Treut, H. L. Greenhouse Gases, Aerosols and Reducing Future Climate Uncertainties. *Surv. Geophys.* **2012**, *33*, 723–731.

(3) Pruppacher, H. R.; Klett, J. D. *Microphysics of Clouds and Precipitation*; Atmospheric and Oceanographic Sciences Library; Springer: Dordrecht, 1978; Vol. 18.

(4) Nel, A. Air Pollution-Related Illness: Effects of Particles. *Science* **2005**, *308*, 804–806.

(5) Cofala, J.; Amman, M.; Klimont, Z.; Kupiainen, K.; Hoglund-Isaksson, L. Scenarios

of Global Anthropogenic Emissions of Air Pollutants and Methane Until 2030. *Atmos. Environ.* **2007**, *41*, 8486–8499.

(6) Mansurov, Z. A. Soot Formation in Combustion Processes (Review). *Combustion, Explosion and Shock Waves* **2005**, *41*, 727–744.

(7) Lack, D. A.; Moosmueller, H.; McMeeking, G. R.; Chakrabarty, R. K.; Baumgardner, D. Characterizing Elemental, Equivalent Black, and Refractory Black Carbon Aerosol Particles: A Review of Techniques, their Limitations and Uncertainties. *Anal. Bioanal. Chem.* **2014**, *406*, 99–122.

(8) Michelsen, H. A. Probing Soot Formation, Chemical and Physical Evolution, and Oxidation: A Review of In Situ Diagnostic Techniques and Needs. *Proceed. Comb. Inst.* **2017**, *36*, 717–735.

(9) Popovicheva, O. B.; Kireeva, E. D.; Steiner, S.; Rothen-Rutishauser, B.; Persiantseva, N. M.; Timofeev, M. A.; Shonija, N. K.; Comte, P.; Czerwinski, J. Microstructure and Chemical Composition of Diesel and Biodiesel Particle Exhaust. *Aerosol Air Qual. Res.* **2014**, *14*, 1392–1401.

(10) Moore, R. H.; Shook, M.; Beyersdorf, A.; Corr, C.; Herndon, S.; Knighton, W. B.; Yu, Z. Influence of Jet Fuel Composition on Aircraft Engine Emissions: A Synthesis of Aerosol Emissions data from the NASA, APEX, AAFEX, and ACCESS Missions. *Energy Fuels* **2015**, *29*, 2591–2600.

(11) Delhaye, D.; Ouf, F.-X.; Ferry, D.; Ortega, I. K.; Penanhoat, O.; Peillon, S.; Salm, F.; Vancassel, X.; Focsa, C.; Irimiea, C.; Harivel, N.; Perez, B.; Quinton, E.; Yon, J.; Gaffie, D. The MERMOSE Project: Characterization of Particulate Matter Emissions of a Commercial Aircraft Engine. *J. Aerosol Sci.* **2017**, *105*, 48–63.

(12) Johnsson, J.; Bladh, H.; Olofsson, N. E.; Bengtsson, P. E. Influence of Soot Aggre-

gate Structure on Particle Sizing Using Laser-Induced Incandescence: Importance of Bridging Between Primary Particles. *Appl. Phys. B* **2013**, *112*, 321–332.

(13) Wang, Y. Y.; Liu, F. S.; He, C. L.; Bi, L.; Cheng, T. H.; Wang, Z. L.; Zhang, H.; Zhang, X. Y.; Shi, Z. B. Fractal Dimensions and Mixing Structures of Soot Particles During Atmospheric Processing. *Environ. Sci. Technol. Lett.* **2017**, *4*, 487–493.

(14) Mosbach, S.; Celnik, M. S.; Raj, A.; Kraft, M.; Zhang, H. R.; Kubo, S.; Kim, K. O. Towards a Detailed Soot Model for Internal Combustion Engines. *Combust. Flame* **2009**, *156*, 1156–1165.

(15) Russo, C.; Alfe, M.; Rouzaud, J. N.; Stanzione, F.; Tregrossi, A.; Ciajolo, A. Probing Structures of Soot Formed in Premixed Flames of Methane, Ethylene and Benzene. *Proceed. Combust. Instit.* **2013**, *34*, 1885–1892.

(16) Botero, M. L.; Adkins, E. M.; Gonzalez-Calera, S.; Miller, H.; Kraft, M. PAH Structure Analysis of Soot in a Non-Premixed Flame Using High-Resolution Transmission Electron Microscopy and Optical Band gap Analysis. *Combust. Flame* **2016**, *164*, 250–258.

(17) Parent, P.; Laffon, C.; Marhaba, I.; Ferry, D.; Regier, T. Z.; Ortega, I. K.; Chazallon, B.; Carpentier, Y.; Focsa, C. Nanoscale Characterization of Aircraft Soot: a High-Resolution Transmission Electron Microscopy, Raman Spectroscopy, X-Ray Photoelecton and Near-Edge X-Ray Absorption Spectroscopy Study. *Carbon* **2016**, *101*, 86–100.

(18) Vander Wal, R. L.; Bryg, V. M.; Hays, M. D. Fingerprinting Soot (Towards Source Identification): Physical Structure and Chemical Composition. *Aerosol Sci.* **2010**, *41*, 108–117.

(19) Herdman, J. D.; Connelly, B. C.; Smooke, M. D.; Long, M. B.; Miller, J. H. A Comparison of Raman Signatures and Laser-Induced Incandescence with Direct Numerical Simulation of Soot Growth in Non-Premixed Ethylene/Air Flames. *Carbon* **2011**, *49*, 5298–5311.

(20) Thrower, P. A. In *The Study of Defects in Graphite by Transmission Electron Microscopy*; Walker Jr., P. L., Ed.; Chemistry and Physics of Carbon; Marcel Dekker: New York, 1969; Vol. 5; pp 217–320.

(21) Stone, A. J.; Wales, D. J. Theoretical Studies of Icosahedral C60 and Some Related Species. *Chem. Phys. Lett.* **1986**, *128*, 501–503.

(22) Stanmore, B. R.; Brilhac, J. F.; Gilot, P. The Oxidation of Soot: A Review of Experiments, Mechanisms and Models. *Carbon* **2001**, *39*, 2247–2268.

(23) Oubal, M.; Picaud, S.; Rayez, M.-T.; Rayez, J.-C. A Theoretical Characterization of the Interaction of Water with Oxidized Carbonaceous Clusters. *Carbon* **2010**, *48*, 1570–1579.

(24) Boukhvalov, D.; Katsnelson, M. I. Chemical Functionalization of Graphene. *J. Phys. Condens. Matter.* **2009**, *21*, 344205.

(25) Banhart, F.; Kotakoski, J.; Krasheninnikov, A. V. Structural Defects in Graphene. *ACSNano* **2010**, *5*, 26–41.

(26) Shiraiwa, M.; Selzle, K.; Pöschl, U. Hazardous Components and Health Effects of Atmospheric Aerosol Particles: Reactive Oxygen Species, Soot, Polycyclic Aromatic Compounds and Allergenic Proteins. *Free Radical Res.* **2012**, *46*, 927–939.

(27) Janssen, N. A. H.; Gerlofs-Nijland, M. E.; Lanki, T.; Salonen, R. O.; Cassee, F.; Hoek, G.; Fischer, P.; Brunekreef, B.; Krzyzanowski, M. In *Health Effects of Black Carbon*; Bohr, R., Ed.; Report from the World Health Organization Regional Office for Europe; 2012.

(28) Bond, T. C. et al. Bounding the Role of Black Carbon in the Climate System: A Scientific Assessment. *J. Geophys. Res. Atmos.* **2013**, *118*, 5380–5552.

(29) Masiol, M.; Harrison, R. M. Aircraft Engine Exhaust Emissions and Other Airport-Related Contributions to Ambient Air Pollution: A Review. *Atmos. Environ.* **2014**, *95*, 409–455.

(30) Butler, K. M.; Mulholland, G. W. Generation and Transport of Smoke Components. *Fire Technol.* **2004**, *40*, 149–176.

(31) Hull, T. R.; Stec, A. A.; Paul, K. T. Hydrogen Chloride in Fires. Proceedings Of The Ninth International Symposium. *Fire Safety Science* **2008**, *9*, 665–676.

(32) Chang, C. T.; Liu, T. H.; Jeng, F. T. Atmospheric Concentrations of the Cl Atom, ClO Radical, and HO Radical in the Coastal Marine Boundary Layer. *Environ. Res.* **2004**, *94*, 67–74.

(33) Andreae, M. O.; Andreae, T. W.; Ferek, R. J.; Raemdonck, H. Long-Range Transport of Soot Carbon in the Marine Atmosphere. *Sci. Tot. Environ.* **1984**, *36*, 73–80.

(34) Popovicheva, O. B.; Kireeva, E. D.; Timofeev, M. A.; Shonija, N. K.; Mogil'nikov, V. P. Carbonaceous Aerosols of Aviation and Shipping Emissions. *Atmos. Ocean. Phys.* **2010**, *46*, 339–346.

(35) Olivié, D. J. L.; Cariolle, D.; Teyssedre, H.; Salas, D.; Voldoire, A.; Clark, H.; Saint-Martin, D.; Michou, M.; Karcher, F.; Balkanski, Y.; Gauss, M.; Dessens, O.; Koffi, B.; Sausen, R. Modeling the Climate Impact of Road Transport, Maritime Shipping and Aviation over the Period 1860-2100 with an AOGCM. *Atmos. Chem. Phys.* **2012**, *12*, 1449–1480.

(36) García Fernández, C.; Radola, B.; Martin-Gondre, L.; Picaud, S.; Rayez, M.-T.; Rayez, J.-C.; Ouf, F.-X.; Rubayo Soneira, J. DFT Study of the Interaction Between Large PAHs and Atomic Chlorine or Hydrogen Chloride Molecule: Toward a Modelling of the Influence of Chlorinated Species on the Trapping of Water by Soot. *Chem. Phys.* **2017**, *483–484*, 46–55.

(37) Hamad, S.; Mejias, J. A.; Lago, S.; Picaud, S.; Hoang, P. N. M. A Theoretical Study of the Adsorption of Water on a Model Soot Surface. I. Quantum Chemical Calculations. *J. Phys. Chem. B* **2004**, *108*, 5405–5409.

(38) Giordana, A.; Maranzana, A.; Ghigo, G.; Causà, M.; Tonachini, G. Soot Platelets and PAHs with an Odd Number of Unsaturated Carbon Atoms and π Electrons: Theoretical Study of Their Spin Properties and Interaction with Ozone. *J. Phys. Chem. A* **2008**, *112*, 973–982.

(39) Giordana, A.; Maranzana, A.; Ghigo, G.; Causà, M.; Tonachini, G. Border Reactivity of Polycyclic Aromatic Hydrocarbons and Soot Platelets Toward Ozone. *J. Phys. Chem. A* **2011**, *115*, 470–481.

(40) Rojas, L.; Peraza, A.; Ruette, F. Aging Oxidation Reactions on Atmospheric Black Carbon by OH Radicals. A Theoretical Modeling Study. *J. Phys. Chem. A* **2015**, *119*, 13038–13047.

(41) Violi, A. Modeling of Soot Particle Inception in Aromatic and Aliphatic Premixed Flames. *Comb. Flame* **2004**, *139*, 279–287.

(42) Violi, A.; Venkatnathan, A. Combustion-Generated Nanoparticles Produced in a Benzene Flame: A Multiscale Approach. *J. Chem. Phys.* **2003**, *125*, 054302.

(43) Qian, H. J.; van Duin, A. C. T.; Morokuma, K.; Irle, S. Reactive Molecular Dynamics Simulation of Fullerene Combustion Synthesis: ReaxFF vs DFTB Potentials. *J. Chem. Theor. Comp.* **2011**, *7*, 2040–2048.

(44) Frisch, M. J. et al. Gaussian 09, Revision A.02, Gaussian, Inc., Wallingford CT. 2016; `www.gaussian.com`.

(45) Dewar, M.; Zoebisch, E.; Healy, E.; Stewart, J. Development and use of quantum me-

chanical molecular models. AM1: A new general purpose quantum mechanical molecular model. *J. Am. Chem. Soc.*. **1985**, *10*, 3902.

(46) Kresse, G.; Hafner, J. Ab Initio Molecular Dynamics for Liquid Metals. *Phys. Rev. B* **1993**, *47*, 558–561.

(47) Kresse, G.; Hafner, J. An Ab Initio Molecular Dynamics Simulation of the Liquid Metal Amorphous Semiconductor Transition in Germanium. *Phys. Rev. B* **1994**, *49*, 14251–14269.

(48) Kresse, G.; Furthmüller, J. Efficiency of Ab Initio Total Energy Calculations for Metals and Semiconductors Using a Plane-Wave Basis Set. *Comput. Mat. Sci.* **1996**, *6*, 15–50.

(49) Kresse, G.; Furthmüller, J. Efficient Iterative Schemes for Ab Initio Total Energy Calculations Using a Plane-Wave Basis Set. *Phys. Rev. B* **1996**, *54*, 11169–11186.

(50) Nosir, M.; Martin-Gondre, L.; Bocan, G.; Muino, R. D. Dissociative Adsorption Dynamics of Nitrogen on a Fe(111) Surface. *Phys. Chem. Chem. Phys.* **2017**, *19*, 24626–24635.

(51) Oubal, M.; Picaud, S.; Rayez, M.-T.; Rayez, J.-C. Interaction of Water Molecules with Defective Carbonaceous Clusters: an Ab Initio Study. *Surf. Sci.* **2010**, *604*, 1666–1673.

(52) Perdew, J. P.; Burke, K.; Ernzerhof, M. Generalized Gradient Approximation Made Simple. *Phys. Rev. Lett.* **1996**, *77*, 3865–3868.

(53) Blöchl, P. E. Projector Augmented-Wave Method. *Phys. Rev. B* **1994**, *50*, 17953–17979.

(54) Kresse, G.; Joubert, D. From Ultrasoft Pseudopotentials to the Projector Augmented-Wave Method. *Phys. Rev. B* **1999**, *59*, 1758–1775.

(55) Monkhorst, H. J.; Pack, J. D. Special Points for Brillouin-Zone Integrations. *Phys. Rev. B* **1976**, *13*, 5188–5192.

(56) Becke, A. D. Density Functional Thermochemistry. III. The Role of Exact Exchange. *J. Chem. Phys.* **1993**, *98*, 5648–5652.

(57) Tachikawa, H.; Iyama, T. Structures and Electronic States of Halogen-Terminated Graphene Nano-Flakes. *Solid State Sci.* **2015**, *50*, 91–96.

(58) Becke, A. D. A New Mixing of Hartree-Fock and Local Density Functional Theory. *J. Chem. Phys.* **1993**, *98*, 1372–1377.

(59) Tsao, M.-L.; Hadad, C. M.; Platz, M. S. Computational Study of the Halogen Atom-Benzene Complexes. *J. Am. Chem. Soc.* **2003**, *125*, 8390–8399.

(60) Montoya, A.; Truong, T. N.; Sarofim, A. F. Spin Contamination in Hartree-Fock and Density Functional Theory Wavefunctions in Modeling of Adsorption on Graphite. *J. Phys. Chem. A* **2000**, *104*, 6108–6110.

(61) Kitchin, J. R. Modeling Materials Using Density Functional Theory. 2012; `http://kitchingroup.cheme.cmu.edu/dft-book/dft.html`.

(62) Liotard, D. A. Algorithmic Tools in the Study of Semiempirical Potential Surfaces. *Int. J. Quant. Chem.* **1992**, *44*, 723–741.

(63) Karlický, F.; Otyepková, E.; Banás, P.; Lazar, P.; Kocman, M.; Otyepka, M. Interplay between Ethanol Adsorption to High-Energy Sites and Clustering on Graphene and Graphite Alters the Measured Isosteric Adsorption Enthalpies. *J. Phys. Chem. C* **2015**, *119*, 20535–20543.

(64) Grimme, S. Semiempirical GGA-Type Density Functional Constructed with a Long-Range Dispersion Correction. *J. Comp. Chem.* **2006**, *27*, 1787–1799.

(65) Jonsson, H.; Millsa, G.; Jacobsen, K. W. In *Classical and Quantum Dynamics in Condensed Phase Simulations*; Berne, B. J., Ciccotti, G., Coker, D. F., Eds.; World Scientific: Singapore, 1998; pp 385–404.

(66) Cabrera-Sanfelix, P.; Darling, G. Dissociative Adsorption of Water at Vacancy Defects in Graphite. *J. Phys. Chem. C* **2007**, *111*, 18258–18263.

(67) Nattino, F.; Diaz, C.; Jackson, B.; Kroes, G. J. Effect of Surface Motion on the Rotational Quadrupole Alignment Parameter of D_2 Reacting on Cu(111). *Phys. Rev. Lett.* **2012**, *108*, 236104.

(68) Nattino, F.; Costanzo, F.; Kroes, G. J. N_2 Dissociation on W(110): An Ab Initio Molecular Dynamics Study on the Effect of Phonons. *J. Chem. Phys.* **2015**, *142*, 104702.

(69) Oubal, M.; Picaud, S.; Rayez, M.-T.; Rayez, J.-C. Water Adsorption on Oxidized Single Atomic Vacancies Present at the Surface of Small Carbonaceous Nanoparticles Modeling Soot. *Chem. Phys. Chem.* **2010**, *11*, 4088–4096.

(70) Suresh, S. J.; Naik, V. M. Hydrogen Bond Thermodynamic Properties of Water from Dielectric Constant Data. *J. Chem. Phys.* **2000**, *113*, 9727–9732.

(71) Picaud, S.; Collignon, B.; Hoang, P. N. M.; Rayez, J.-C. Molecular Dynamics Simulation Study of Water Adsorption on Hydroxylated Graphite Surfaces. *J. Phys. Chem. B* **2006**, *110*, 8398–8408.

(72) Picaud, S.; Collignon, B.; Hoang, P. N. M.; Rayez, J.-C. Adsorption of Water Molecules on Partially Oxidized Graphite Surfaces: a Molecular Dynamics Study of the Competition Between OH and COOH Sites. *Phys. Chem. Chem. Phys.* **2008**, *10*, 6998–7009.

(73) Nguyen, V. T.; Do, D. D.; Nicholson, D. A New Molecular Model for Water Adsorption on Graphitized Carbon Black. *Carbon* **2014**, *66*, 629–636.

(74) Mocho, V. M.; Ouf, F.-X. Clogging of Industrial Pleated High Efficiency Particulate Air (HEPA) Filters in the Event of Fire. *Nucl. Eng. Des.* **2011**, *241*, 1785.

(75) Ouf, F.-X.; Mocho, V. M.; Pontreau, S.; Wang, Z.; Ferry, D.; Yon, J. Clogging of Industrial High Efficiency Particulate Air (HEPA) Filters in Case of Fire: From Analytical to Large-Scale Experiments. *Aerosol Sci.* **2014**, *48*, 939.

(76) Ouf, F.-X.; Mocho, V. M.; Pontreau, S.; Wang, Z.; Ferry, D.; Yon, J. Physicochemical Properties of Aerosol Released in the Case of a Fire Involving Materials Used in the Nuclear Industry. *J. Hazard. Mater.* **2015**, *283*, 340.

Graphical TOC Entry